Nanoscale Research Letters

NANO EXPRESS Open Access

Tantalum disulfide quantum dots: preparation, structure, and properties

Liangliang Zhou[1], Chuli Sun[3], Xueming Li[1*], Libin Tang[2*], Wei Guo[3*], Lin Luo[2], Meng Zhang[4], Kar Seng Teng[5], Fuli Qian[1], Chaoyu Lu[1], Jing Liang[1], Yugui Yao[3] and Shu Ping Lau[6]

Abstract

Tantalum disulfide (TaS_2) two-dimensional film material has attracted wide attention due to its unique optical and electrical properties. In this work, we report the preparation of 1 T-TaS_2 quantum dots (1 T-TaS_2 QDs) by top-down method. Herein, we prepared the TaS_2 QDs having a monodisperse grain size of around 3 nm by an effective ultrasonic liquid phase exfoliation method. Optical studies using UV-Vis, PL, and PLE techniques on the as-prepared TaS_2 QDs exhibited ultraviolet absorption at 283 nm. Furthermore, we found that dimension reduction of TaS_2 has led to a modification of the band gap, namely a transition from indirect to direct band gap, which is explained using first-principle calculations. By using quinine as reference, the fluorescence quantum yield is 45.6%. Therefore, our results suggest TaS_2 QDs have unique and extraordinary optical properties. Moreover, the low-cost, facile method of producing high quality TaS_2 QDs in this work is ideal for mass production to ensure commercial viability of devices based on this material.

Keywords: Transition metal dichalcogenides, Quantum dots, Ultrasonic method, First-principle, Modulating bandgap

Introduction

Recently, the family of layered transition metal dichalcogenides (LTMDs) [1] has drawn great attention in many fields, such as electronic devices [2], energy storage [3], catalysis [4], bio-imaging [5, 6], and biosensing [7], due to its many interesting physical and electrical properties. Typically, the structure of LTMDs is formed [1] by covalently bonded monolayer, and each monolayer is linked by Van der Waals forces; hence the LTMDs can be easily cleaved along the layer plane by either chemical or physical methods. According to previous work, the band gaps of LTMDs can be modified from indirect to direct band gap by decreasing the number of layers [8]. In particular, the TaS_2 has been studied extensively for various applications, ranging from optical switch [9] to catalysis [10], as they exhibit tunable band gap, controllable size, and strong photoluminescence. Therefore, it is becoming a widely focused functional material.

At present, both top-down and bottom-up methods are adopted to prepare nanomaterials [11, 12]. The bottom-up approach is based on atoms and molecules as building blocks, which are used to form nanoparticle structures according to relevant purposes. This method mainly involves gas-phase and liquid-phase reactions [13, 14]. As for the top-down approach, electrochemical and etching methods [15, 16] have been applied to prepare TaS_2 nanomaterials by weakening the Van der Waals interactions and cleaving the bonding force between the layers to obtain TaS_2 nanomaterials from its bulk materials. For example, Zeng et al. [17] prepared TaS_2 nanosheets through lithium interaction and exfoliation by controlling the cut-off voltage. Zhang et al. [18] prepared monodispersed TaS_2 nanodots by a facile top-down method. QDs [19–22] has attracted wide interest worldwide in recent years, but TaS_2 QDs are rarely reported. Therefore, facile methods are still in need to prepare industry applicable TaS_2 QDs with narrow size distribution and good dispersion.

* Correspondence: lxmscience@163.com; scitang@163.com; weiguo7@bit.edu.cn
[1]Key Laboratory of Advanced Technique & Preparation for Renewable Energy Materials, Ministry of Education, Yunnan Normal University, Kunming 650500, People's Republic of China
[2]Kunming Institute of Physics, Kunming 650223, People's Republic of China
[3]School of Physics, Beijing Institute of Technology, Beijing 100081, People's Republic of China
Full list of author information is available at the end of the article

In this study, TaS_2 QDs with a monodisperse grain size of around 3 nm were prepared by ultrasonic method. In this process, the Van der Waals interactions in between the TaS_2 layers were first weakened by intercalation of NMP and then followed by further exfoliation using high power ultrasonic energy. The size of TaS_2 QDs can be easily tuned by adjusting centrifugation rate and time; a higher centrifugation rate and a bigger centrifugation time result in a smaller size. This provides an efficient and practical method in the preparation of TaS_2 QDs. Its structural, electronic, and optical properties were characterized by experiments, as well as first-principle calculations.

Methods

The TaS_2 powder was purchased from Aladdin Company (Chengdu China, purity ≥ 99.99%). The chemical reagents were purchased from Sinopharm Chemical Reagent Co. Ltd and used as received: N-methyl-2-pyrritolidone (NMP) (purity ≥ 99.0%) and ethanol (purity ≥ 99.7%).

Preparation of TaS_2 QDs

TaS_2 powder 0.5 g was grinded in the mortar for 2 h. Fifty milliliters of NMP solvent was added to the grinded powder sample. The mixture was then ultrasonic treated for 4 h with an ultrasonic power of 210 W. The suspension after ultrasonic treatment was centrifuged at the rate of 7000 rpm for 25 min. The supernatant, which obtains the TaS_2 QDs, was collected.

General Characterization

The morphology, elemental composition, and size distribution of TaS_2 QDs were studied using transmission electron microscopy (TEM, Tecnai G2 TF30 S-Twin), atomic force microscopy (AFM, Seiko SPA-400), scanning electron microscopy (SEM, SUPRA 55VP), and energy-dispersive spectroscopy (EDS, X-Max20). TaS_2 QDs suspension was drop-casted onto an ultrathin carbon-coated holey support film, consisting of 300 mesh copper grids, during TEM characterization. The phase structure of TaS_2 QDs was characterized by X-ray photoelectron microscopy (XPS, PHI Versa probe II), X-ray diffractometer (XRD, UItima IV, X-ray source: Cu Kα, λ = 1.54178 Å), Fourier-transform infrared spectrometer (FTIR, Nicolet iS10) using the KBr pellet technique, and Raman spectroscopy (Renishaw in Via) using an argon-ion laser having an excitation wavelength of 514.5 nm. The optical properties of TaS_2 QDs were characterized using UV-visible spectrophotometer (UV-Vis, Shimadzu UV-3600) and fluorescence photoluminescence spectrometer (PL and PLE, Hitachi, F-4500).

Results and Discussion

The process of TaS_2 QDs formation from its bulk crystal is depicted in Fig. 1a. The preparation process consisted of three steps, namely grinding, ultrasonic, and centrifugation. An enlarged schematic of TaS_2 QDs is shown within the dotted red square of Fig. 1a. The tawny solution in the sample bottle was TaS_2 QDs solution after centrifugation. Figure 1 b shows the TEM image of the TaS_2 QDs, which are spherical in shape with uniform

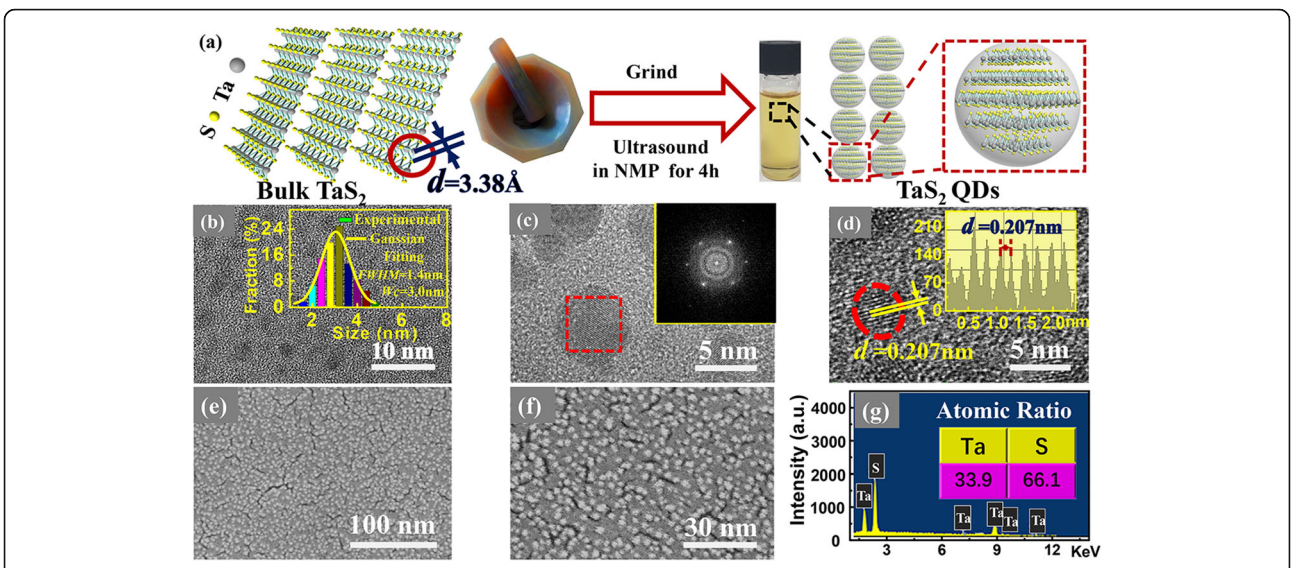

Fig. 1 **a** Schematic diagram showing the process of TaS_2 QDs formation; **b** TEM image of the TaS_2 QDs, inset shows TaS_2 QDs particle size distribution. Gaussian fitting curve is shown as yellow line; **c** FFT pattern (inset) of a selected area (dotted red square); **d** HR-TEM image of the TaS_2 QDs, inset shows the line profile of the diffraction fringes; **e** SEM image at 70.0 K; **f** SEM image at 100.0 K; **g** EDS spectrum of TaS_2 QDs

size distribution. As shown in the inset, the size distribution of the TaS_2 QDs followed a Gaussian fitted curve with an average diameter of W_C = 3.0 nm and full width at half maximum (*FWHM*) of 1.4 nm. It was reported that the thickness of the TaS_2 monolayer ranged from 0.6 to 1.2 nm [23]; hence, the QDs could comprise of 2–5 layers of TaS_2. The number of TaS_2 layer can be reduced by increasing the centrifugal rate and time (as shown in Additional file 1: Fig. S1).

The FFT pattern is shown in the inset of Fig. 1c. It shows a hexagonal crystalline structure, which corresponds to the TaS_2 QDs structure in Fig. 1a. As shown in Fig. 1d, the TaS_2 QDs line profile exhibits obvious lattice stripe with a spacing of 0.207 nm. The SEM image in Fig. 1e shows a uniform distribution of TaS_2 QDs, thus indicating a good dispersibility and uniform size distribution. At higher SEM magnification, it is apparent that the surface consisted of rugged particles as shown in Fig. 1f. This indicates the formation of independent spherical TaS_2 QDs during the preparation process. EDS technique was used to characterize the elemental composition as shown in Fig. 1g. A film of TaS_2 QD_S was deposited on copper sheet during the EDS characterization in order to avoid the overlapping of Ta and Si/SiO_2 substrate peaks, which could complicate the analysis. The measured atomic percentage ratio of Ta and S in the material was 33.9/66.1 ≈ 1:1.95, which is close to the theoretical value of 1:2.

Figure 2 a shows AFM images of the TaS_2 QDs, labeled as A, B, and C, which were randomly selected and their heights were measured to be 2.30 nm, 2.03 nm, and 2.91 nm, respectively. The average height of 2.41 nm is consistent with the average diameter of 3.01 nm measured using TEM. The FTIR spectra, shown in Fig. 2b, reveal that the Ta-S bond stretching vibration absorption peak was situated at 616 cm^{-1}. Figure 2 c shows Ta 4*f*, S 2*p*, ★C 1*s*, and ★O 1*s* peaks from XPS full-scan spectrum. The ★C 1*s* and ★O 1*s* peaks were impurity

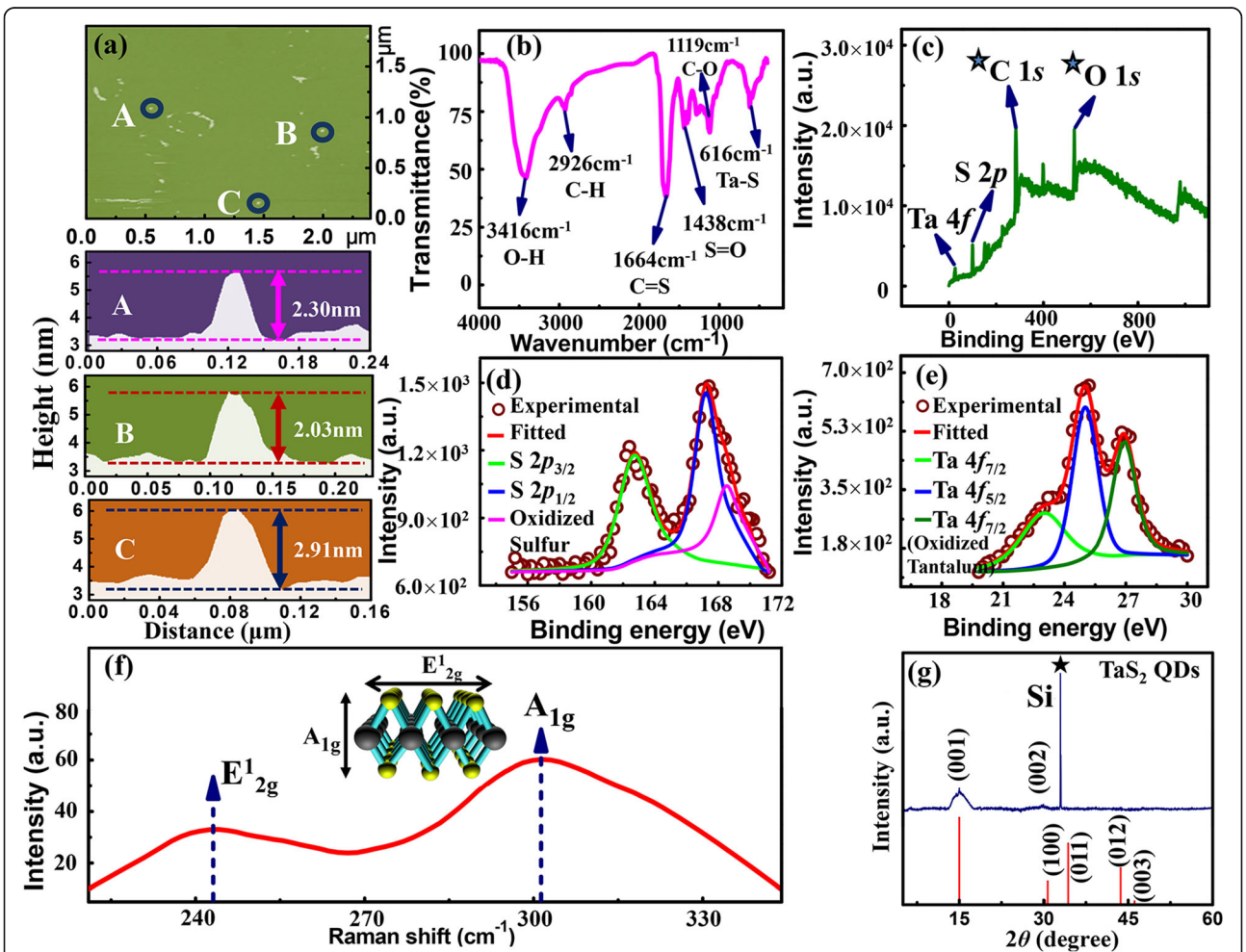

Fig. 2 **a** AFM morphology and height analysis results of TaS_2 QDs, labeled A, B and C, were randomly selected three points; **b** TaS_2 QDs FTIR spectrum; **c** the full-scan XPS spectrum of the TaS_2 QDs; **d** XPS spectrum of S 2*p*; **e** XPS spectrum of Ta 4*f*; **f** The Raman vibration mode of TaS_2 QDs and Raman spectra of TaS_2 QDs; **g** XRD diffraction pattern of TaS_2 QDs

peaks produced by solvent NMP and oxide. Figure 2 d shows the XPS spectrum of S 2*p* deconvoluted into three components, namely S $2p_{3/2}$ (163.4 eV), S $2p_{1/2}$ (166.7 eV), and oxidized sulfur (168.2 eV). The XPS spectrum of Ta 4*f* is shown in Fig. 2e and was deconvoluted into components, such as Ta $4f_{7/2}$ (23.2 eV), Ta $4f_{5/2}$ (25.6 eV), and Ta $4f_{7/2}$ (27.2 eV). The Ta $4f_{7/2}$ peak at 27.2 eV is associated with oxidized tantalum [24, 25]; oxidation has also been observed in other QDs [26–28]. Figure 2 f shows the Raman vibration mode of TaS_2 QDs. The E^1_{2g} and A_{1g} modes relate to the in-plane and out-of-plane vibration respectively [29]. The A_{1g} and E^1_{2g} modes of the TaS_2 QDs were observed at 301.4 cm^{-1} and 242.3 cm^{-1} respectively. The Raman intensity of the E^1_{2g} vibration mode was much smaller than that of A_{1g}, which could due to the fact that A_{1g} mode is more sensitive to strain than the E^1_{2g} mode in TaS_2 QDs. It shows that the A_{1g} mode dominated during the preparation process of TaS_2 QDs. Figure 2 g shows XRD diffraction pattern of the TaS_2 QDs. When compared with space group $P\bar{3}m1$(164), the pattern indicates trigonal structure of 1 T-TaS_2 [30]. According to the standard PDF#04-001-0068 card, the diffraction peak 2θ at 15.0° represented crystal plane (001) with d = 0.590 nm, which corresponds to the *C*-axis crystal surface spacing. The peak at 30.2° represented crystal plane (002) with d = 0.295 nm. The peak at 33.0° (asterisk peak) was originated from the Si (001) substrate [31]. The grain size can be calculated using the Debye-Scherrer (Eq. (1)) [32].

$$D = \frac{0.89\lambda}{\beta \cos\theta} \tag{1}$$

where D is grain size, β is *FWHM* of the diffraction peak of the measured sample, θ is diffraction angle, and λ is X-ray wavelength. The calculated grain size of 3.8 nm using the strongest diffraction peak (001) is close to the TEM result of 3.01 nm. Figure 3 a and d show the PL and PLE spectra of the TaS_2 QDs respectively, with excitation wavelength (λ_{Ex}) varied from 320 nm to 460 nm and the emission wavelength (λ_{Em}) changed from 400 to 520 nm at 20 nm step. The PL and PLE peaks were red-shifted, as indicated by the dark blue lines in Fig. 3a and d respectively. As shown in Fig. 3b and e, the red-shift of the normalized intensity peaks is more noticeable for the PL (e.g., from 391 to 519 nm) than the PLE (e.g., from 324 to 380 nm) spectra. The wavelength and energy-dependent PL and PLE peaks are shown in greater details in Fig. 3c and f respectively. The peak energies of the red-shifted excitation wavelength ranged from 3.17 to 2.39 eV, while the red-shifted emission energies ranged from 3.83 to 3.26 eV. It can be seen that a higher excitation energy (λ_{Ex} = 320 nm) led to a larger Stokes shift (71 nm), whereas a lower excitation energy (λ_{Ex} = 460 nm) resulted in a smaller Stokes shift (59 nm). The difference in Stokes shift is probably due to the size distribution of the prepared QDs, which has also been observed from Se QDs and Te QDs [27, 28]. Comparing the PL and PLE peaks,

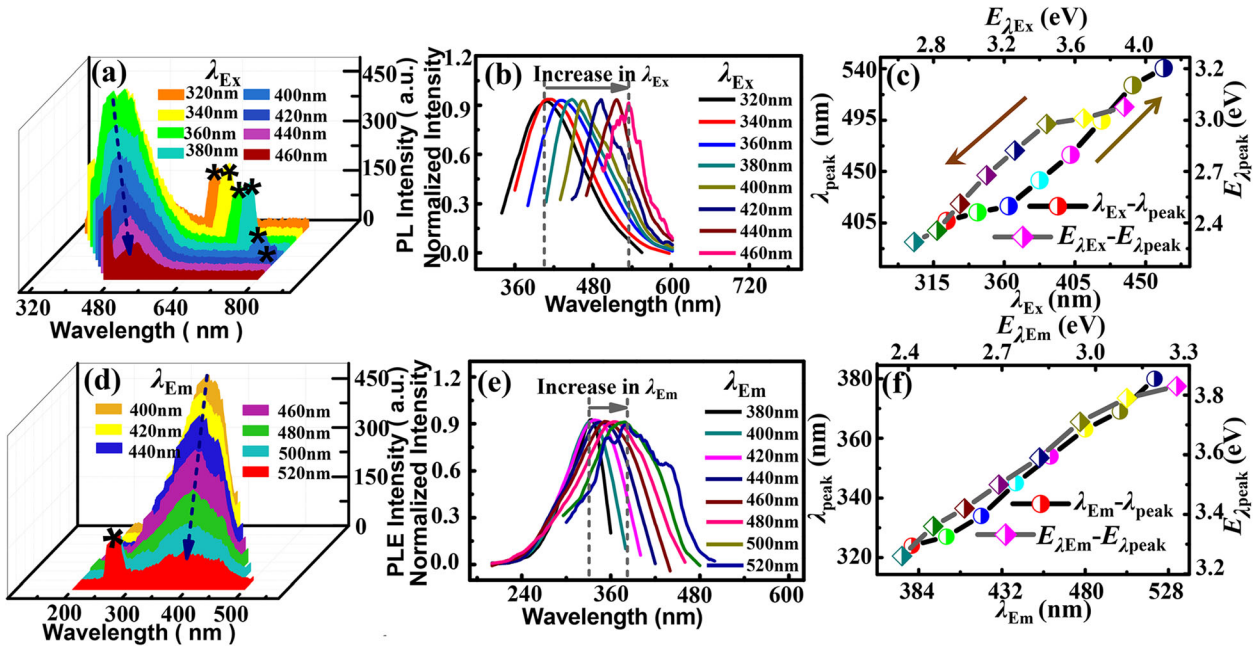

Fig. 3 **a**, **d** The PL & PLE spectra of TaS_2 QDs [* interference peak (λ_{Ex} and λ_{Em}) from the instrument], respectively; **b**, **e** The PL and PLE normalized spectra of TaS_2 QDs under different λ_{Ex} and λ_{Em}, respectively; **c**, **f** the relationship of peak and energy for TaS_2 QDs

the PL peaks exhibited a greater red-shift than the PLE peaks, and with the increase of the peak wavelengths, the PL peak has a larger Stokes frequency shift than the PLE peak [33]. The red-shifted intensity peak indicates that the optical properties of TaS_2 QDs have an obvious dependence on the wavelength.

Figure 4a shows the UV-Vis absorption spectra of TaS_2 QDs. An absorption peak was observed at 283 nm, which is caused by electron transition upon UV illumination. Based on the study of the reduction in the number of layers, a blue-shifted absorption peak was observed (as shown in Additional file 1: Fig. S2). In addition, the TaS_2 QDs solution appeared yellow in color under natural light, peony in color under ultraviolet at 254 nm, and blue in color at 365 nm. Tauc mapping method was used to calculate the TaS_2 QDs' band gap spectrum, according to Eq. (2) [17, 34]:

$$\alpha \mathrm{hv} = A\left(\mathrm{hv} - E_g\right)^{1/2} \tag{2}$$

where α is absorption coefficient, A is a constant, hv is light energy, and E_g is band gap energy. The TaS_2 QDs has a direct band gap (E_g = 3.69 eV) as shown in Fig. 4b. The results indicate a reduction in the number of layers in TaS_2 QDs would lead to a modification of the band gap, including indirect to direct band gap transitions. Based on the above results, TaS_2 QDs energy level structure is proposed as shown in Fig. 4c. During electron transition ($E1$-$E2$), the energy level of TaS_2 QDs is E_g = 4.38 eV. Due to the presence of surface energy level, an emission wavelength of 401 nm is observed and this corresponds to E_g = 3.09 eV. Therefore, the transition energy from $E1$ to surface state is about 1.3 eV. In order to study the influence of fluorescence effect caused by the increase in band gap, the fluorescence quantum yield (Q_s) of TaS_2 QDs was calculated using quinine (Q_r= 0.54 in 24.9% ethanol) as reference, based on the following equation (Eq. 3) [35, 36]:

$$Q_s = Q_r \times \frac{I_s}{I_r} \times \frac{A_r}{A_s} \times \left(\frac{n_s}{n_r}\right)^2 \tag{3}$$

where the subscript $_s$ denotes sample and $_r$ indicates reference. $_Q$ is PL quantum yield, $_I$ is emitting peak area of fluorescence, A is absorbance at a specific excitation wavelength, and n is refractive index. The calculated fluorescenceyield of 45.6% indicates excellent fluorescence properties of the TaS_2 QDs. First-principle calculations were performed to further investigate the reasons for the increase in band gap of TaS_2 QDs. Figure 5 a and b show the bulk and monolayer structures of TaS_2. For the monolayer TaS_2, a vacuum of 29.5 Å in the Z direction was added when constructing the unit-cell. The calculations were performed using density functional theory (DFT) as implemented in the Vienna Ab initio simulation package (VASP) [37–39]. The electronic exchange-correlation effects were treated using the generalized gradient

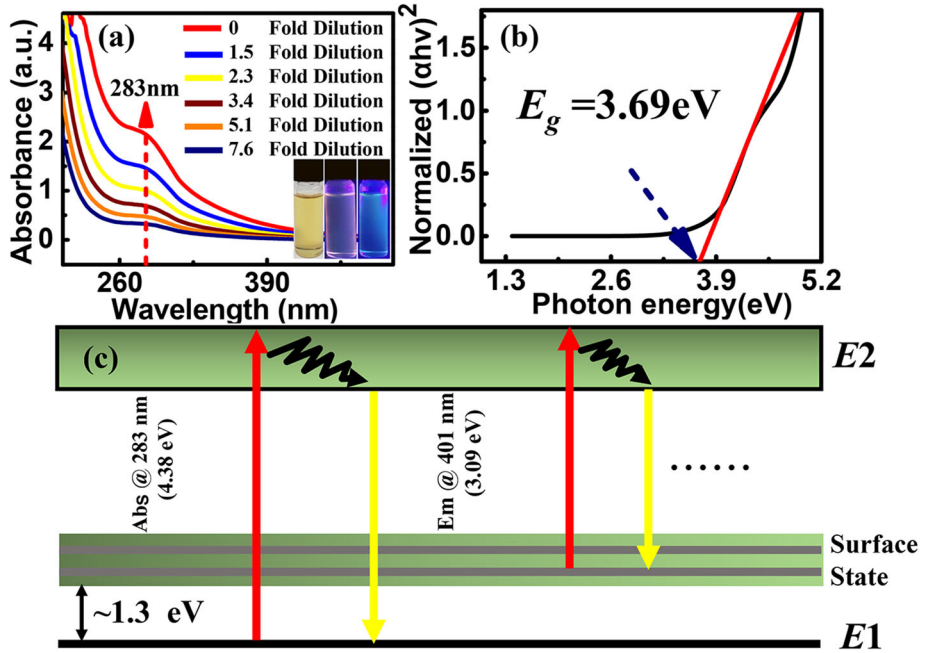

Fig. 4 **a** UV-Vis absorption spectra of TaS_2 QDs and TaS_2 QDs in natural light, 254 nm and 365 nm UV light illumination; **b** the direct band gap spectrum of the TaS_2 QDs by Tauc method; **c** energy level diagram of TaS_2 QDs

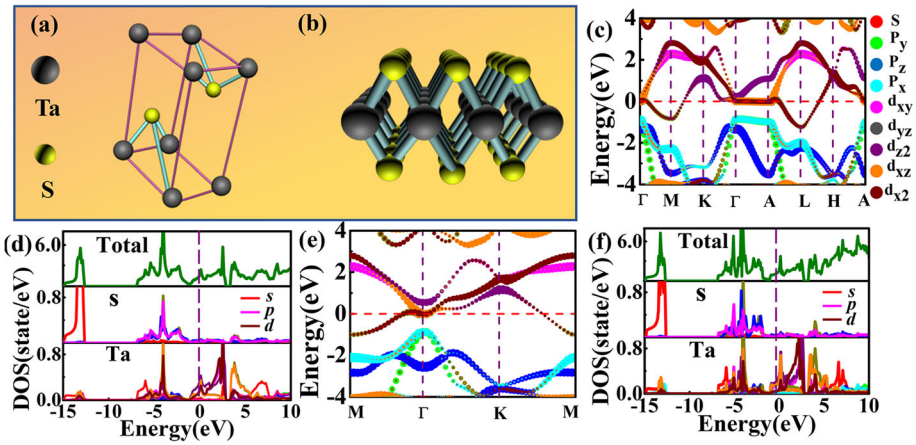

Fig. 5 Structure of TaS_2, **a** bulk TaS_2 and **b** monolayer TaS_2. **c**–**f** Band structure calculations by PBE functional. Partial band structures of bulk and monolayer TaS_2 in **c** and **e**, respectively. Partial density of states (PDOS) of bulk and monolayer TaS_2 in **d** and **f**, respectively

approximation (GGA) in the Perdew-Burke-Ernzerhof (PBE) form [40, 41]. When using Heyd-Scuseria-Ernzerhof (HSE) hybrid functionals [42, 43], 25% Hartree-Fock and 75% PBE-GGA were chosen for short-ranged exchange part in the HSE06 hybrid functionals. The projector augmented wave (PAW) method was utilized to treat the interactions between the ionic cores and the valence electrons [44, 45], where valence electron configuration of S and Ta were set as $3S^2 3p^4$ and $5d^3 6s^2$, respectively. The energy cut-off of plane wave basis was set to 520 eV. The Monkhorst-Pack grid mesh [46] of 11 × 11 × 7 and 11 × 11 × 1 were used to sample the Brillouin zone of the bulk and monolayer TaS_2, respectively. The convergence in energy was set to 1×10^{-5} eV during electronic structure calculations. The electronic structures of bulk and monolayer TaS_2 were calculated by PBE functional, as shown in Fig. 5c and e, respectively.

The results are in good agreement with previous calculations [47, 48]. Both the bulk and monolayer TaS_2 have metallic in-phase states, and the band across the Fermi level is mostly composed of d_{x2} orbital of Ta atoms. The valence band is mainly composed of p orbitals of S atoms, while the conduction band is mainly from d orbitals of Ta atoms. At Γ point, an indirect gap is transiting to a direct gap from bulk to monolayer structure due to lacking of inter-plane interactions. The band structure was checked using HSE06 hybrid functionals (Fig. 6a, b). The results are similar to PBE except for a larger gap near Γ point for the HSE results, where the conduction band shifted toward lower energy for about 0.5 eV. The absorption spectrum of monolayer TaS_2 was also calculated and it contains mainly four peaks at 1.41 eV, 2.00 eV, 6.61 eV, and 7.23 eV. Comparing the

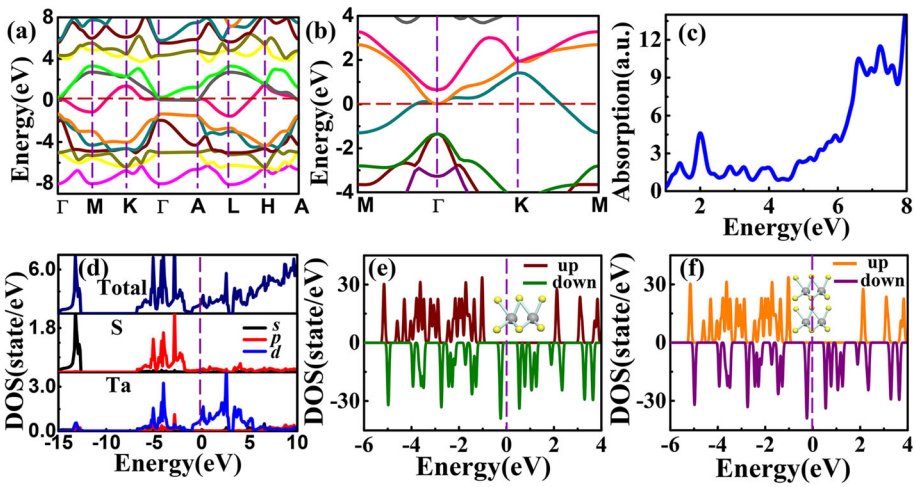

Fig. 6 **a** Bulk and **b** monolayer TaS_2 by HSE functionals. **c** Optical absorption spectra of monolayer TaS_2. **d** PDOS by calculated by HSE. **e** The monolayer and **f** the two-layer DOS of QDs calculated by HSE

absorption spectra and the PDOS, as shown in Fig. 6c and d, the two peaks in the 0~2 eV region are provided by the S 3*p*→Ta 5*d* electronic transitions, and the S 3*p* → Ta 6 *s* electronic transitions contribute to the peaks in the 6~8 eV region.

Next, the TaS_2 QDs were modeled as clusters with one and two-layer of Ta-2S unit and compared their spin-polarized DOS. As shown in Fig. 6e and f, due to the dangling bonds of S atoms at the surface, the spin-polarized DOS of the one- and two-layer models show half-metallic nature, where there is a ~ 3 eV gap for the spin-up electrons that is twice the gap at Γ point of the infinite 2D monolayer in Fig. 6b. This demonstrates strong quantum confinement effect. The gap of spin-up electrons of the one-layer model is slightly larger than the two-layer model as a result of lacking inter-plane interactions.

Conclusions

TaS_2 QDs having an average size of about 3 nm were prepared by ultrasonic method. The morphology and structural studies performed on the nanomaterials show that they have controllable and hexagonal honeycomb shape. The optical properties of the TaS_2 QDs, including absorption and PL, were investigated. A red-shifted effect, compared to the bulk material, was observed and the QDs exhibited multicolor luminescence with strong absorption in near ultraviolet region. The band gap of the TaS_2 QDs increased to 3.69 eV from indirect to direct band gap, hence exhibiting extraordinary optical properties. The indirect to direct transition and quantum confinement effect in the electronic structures were confirmed by first-principle calculations of a simple model of the QDs. These results will extend the application of TaS_2 QDs in devices, such as photodetectors. Furthermore, the preparation method is also applicable to other layered materials to produce low-cost high-quality QDs from bulk materials.

Supplementary information

Supplementary information accompanies this paper at https://doi.org/10.1186/s11671-020-3250-1.

Additional file 1: Fig. S1. (a) and **(c)** show the HR-TEM images of the TaS_2 QDs after centrifugation at 16000 rpm for 30 minutes. **(b)** Particle size distribution of TaS_2 QDs. **(d)** The line profile of the TaS_2 QDs diffraction fringes. **Fig. S2. (a)** UV-Vis absorption spectra of TaS_2 QDs after centrifugation at 16000 rpm for 30 minutes. **(b)** UV-Vis absorption spectra of TaS_2 QDs compared between 16000 rpm for 30 minutes and 7000 rpm for 25 minutes. **(c)** and **(d)** show normalized PL spectra of TaS_2 QDs with excitation wavelength (λ_{Ex}) of 250 nm and 270 nm, respectively.

Abbreviations

AFM: Atomic force microscopy; EDS: Energy-dispersive spectroscopy; FTIR: Fourier-transform infrared spectrometer; LTMDs: Layered transition metal dichalcogenides; NMP: N-methyl-2-pyrritolidone; PL and PLE: Fluorescence photoluminescence spectrometer; SEM: Scanning electron microscopy; TaS_2: Tantalum disulfide; TEM: Transmission electron microscopy; UV-Vis: UV-visible spectrophotometer; XPS: X-ray photoelectron microscopy; XRD: X-ray diffraction

Authors' Contributions

XML and LBT designed and supervised the experiments. WG supervised the simulations. LLZ carried out the experiments. CLS carried out the simulations. LL, MZ, FLQ, CYL, and JL carried out the characterizations. KST, YGY, and SPL interpreted the results and improved the manuscript. All authors read and approved the final manuscript.

Funding

This work has been supported by the National Natural Science Foundation of China (Grant Nos. 51462037 and 61106098), the Key Project of Applied Basic Research of Yunnan Province, China (Grant No. 2012FA003), and Fundamental Research Funds for the Central Universities (Grant No. 2017CX10007).

Availability of Data and Materials

The data supporting the conclusions of this article are included within the article and its additional files.

Ethics Approval and Consent to Participate

Not applicable

Competing Interests

The authors declare that they have no competing interests.

Author details

[1]Key Laboratory of Advanced Technique & Preparation for Renewable Energy Materials, Ministry of Education, Yunnan Normal University, Kunming 650500, People's Republic of China. [2]Kunming Institute of Physics, Kunming 650223, People's Republic of China. [3]School of Physics, Beijing Institute of Technology, Beijing 100081, People's Republic of China. [4]Institute of Environment and Health, Jianghan University, Wuhan 430056, People's Republic of China. [5]Teng College of Engineering, Swansea University, Bay Campus, Fabian Way, Swansea SA1 8EN, UK. [6]Department of Applied Physics, The Hong Kong Polytechnic University, Hong Kong, SAR, People's Republic of China.

Received: 8 November 2019 Accepted: 6 January 2020
Published online: 28 January 2020

References

1. Wang H, Yuan H, Sae HS, Li Y, Cui Y (2015) Physical and chemical tuning of two-dimensional transition metal dichalcogenides. Chem Soc Rev 44:2664–2680
2. Desjardins MM, Viennot JJ, Dartiailh MC, Bruhat LE, Delbecq MR, Lee M, Choi M-S, Cottet A, Kontos T (2017) Observation of the frozen charge of a Kondo resonance. Nature 545:71–74
3. Wei Q, Xiong F, Tan S, Huang L, Lan EH, Dunn B, Mai L (2017) Porous one-dimensional nanomaterials: design, fabrication and applications in electrochemical energy storage. Adv Mater 29:1602300–1602339
4. Liu P, Qin R, Fu G, Zheng N (2017) Surface coordination chemistry of metal nanomaterials. J Am Chem Soc 139:2122–2131
5. Zhou K, Zhang Y, Xia Z (2016) As-prepared MoS_2 quantum dot as a facile fluorescent probe for long-term tracing of live cells. Nanotechnology 27:275101
6. Zebibula A, Alifu N, Xia L, Sun C, Yu X, Xue D, Liu L, Li G, Qian J (2018) Ultrastable an biocompatible NIR-II quantum dots for functional bioimaging. Adv Funct Mater 28:1703451–1703463
7. Bollella P, Fusco G, Tortolini C, Sanzò G, Favero G, Gorton L, Antiochia R (2017) Beyond graphene: electrochemical sensors and biosensors for biomarkers detection. Biosens Bioelectron 89:152–166
8. Zhao R, Wang Y, Deng D, Luo X, Lu WJ, Sun Y-P, Liu Z-K, Chen L-Q, Robinson J (2017) Tuning phase transitions in TaS_2 via the substrate. Nano Lett 17:3471–3477
9. Perfetti L, Loukakos PA, Lisowski M (2006) Time evolution of the electronic structure of 1 T-TaS_2 through the insulator-metal transition. Phys Rev Lett 97:067402
10. Li H, Lu G, Wang Y, Yin Z, Cong C, He Q, Zhang H (2013) Mechanical exfoliation and characterization of single-and few-layer nanosheets of WSe_2, TaS_2, and $TaSe_2$. Small 9:1974–1981

11. Zhu S, Song Y, Wang J, Wan H, Zhang Y, Ning Y, Yang B (2017) Photoluminescence mechanism in graphene quantum dots: quantum confinement effect and surface/edge state. Nano Today 13:10–14
12. Gazibegovic S, Car D, Zhang H, Balk SC, Logan JA, de Moor MW, Cassidy MC, Schmits R, Xu D, Wang G, Krogstrup P (2017) Epitaxy of advanced nanowire quantum devices. Nature 548:434–438
13. Mateo D, Albero J, García H (2017) Photoassisted methanation using Cu_2O nanoparticles supported on graphene as a photocatalyst. Energy Environ Sci 10:2392–2400
14. Bonaccorso F, Colombo L, Yu G, Stoller M, Tozzini V, Ferrari AC, Ruoff RS, Pellegrini V (2015) 2D materials. graphene, related two-dimensional crystals, and hybrid systems for energy conversion and storage. Science 347: 1246501–1246511
15. Thompson, A. H.: Electrochemical studies of lithium intercalation in titanium and tantalum dichalcogenides. Physica B + C 99, 100-106 (1980). DOI:10. 1016/0378-4363(80)90216-8
16. Wu J, Peng J, Yu Z, Zhou Y, Xie Y (2017) Acid-assisted exfoliation toward metallic sub-nanopore TaS_2 monolayer with high volumetric capacitance. J Am Chem Soc 140:493–498
17. Zeng Z, Tan C, Huang X, Bao S, Zhang H (2014) Growth of noble metal nanoparticles on single-layer TiS_2 and TaS_2 nanosheets for hydrogen evolution reaction. Energy Environ Sci 7:797–803
18. Zhang X, Lai Z, Liu Z, Tan C, Huang Y, Li B (2015) A facile and universal top-down method for preparation of monodisperse transition-metal dichalcogenide nanodots. Angew Chem Int Ed 54:5425–5428
19. Zhu J, Yan X, Cheng J (2018) Synthesis of water-soluble antimony sulfide quantum dots and their photoelectric properties. Nanoscale Res Lett 13:19
20. Li R, Tang L, Zhao Q, Ly TH, Teng KS, Li Y, Lau SP (2019) In_2S_3 Quantum dots: preparation, properties and optoelectronic application. Nanoscale Res Lett 14:161
21. Ramanery FP, Mansur AA, Mansur HS, Carvalho SM, Fonseca MC (2016) Biocompatible fluorescent core-shell nanoconjugates based on chitosan/ Bi_2S_3 quantum dots. Nanoscale Res Lett 11:187
22. Kim JI, Kim J, Lee J, Jung DR, Kim H, Choi H, Park B (2012) Photoluminescence enhancement in CdS quantum dots by thermal annealing. Nanoscale Resh Lett 7:482
23. Pan J, Guo C, Song C, Lai X, Li H, Zhao W, Zhang H, Mu G, Bu K, Lin T, Xie X, Chen M, Huang F (2017) Enhanced superconductivity in restacked TaS_2 nanosheets. J Am Chem Soc 139:4623–4626
24. Chang JP, Steigerwald ML, Fleming RM, Opila RL, Alers GB (1999) Thermal stability of Ta_2O_5 in metal–oxide–metal capacitor structures. Appl Phys Lett 74:3705–3707
25. Peters ES, Carmalt CJ, Parkin IP, Tocher DA (2005) Aerosol-assisted chemical vapor deposition of NbS_2 and TaS_2 thin films from pentakis (dimethylamido) metal complexes and 2-methylpropanethiol. Eur J Inorg Chem 2005:4179–4185
26. Li X, Lau SP, Tang L, Ji R, Yang P (2014) Sulphur doping: a facile approach to tune the electronic structure and optical properties of graphene quantum dots. Nanoscale 6:5323–5328
27. Qian F, Li X, Tang L, Lai SK, Lu C, Lau SP (2017) Selenium quantum dots: preparation, structure, and properties. Appl Phys Lett 110:053104
28. Lu C, Li X, Tang L, Lai SK, Rogée L, Teng KS, Qian F (2017) Zhou. L. & Lau, S. P.: Tellurium quantum dots: preparation and optical properties. Appl Phys Lett 111:063112–063117
29. Jeong H, Oh HM, Gokarna A, Kim H, Yun SJ, Han GH, Jeong MS, Lee YH, Lerondel G (2017) Integrated freestanding two-dimensional transition metal dichalcogenides. Adv Mater 29:1700308–1700317
30. Dunnill CW, Edwards HK, Brown PD, Gregory DH (2006) Single-step synthesis and surface-assisted growth of superconducting TaS_2 nanowires. Angew Chem Int Edit 45:7060–7063
31. MacIsaac C, Schneider JR, Closser RG, Hellstern TR, Bergsman DS, Park J, Bent SF (2018) Atomic and molecular layer deposition of hybrid Mo–Thiolate thin films with enhanced catalytic activity. Adv Funct Mater 28: 1800852
32. Holzwarth U, Gibson N (2011) The Scherrer equation versus the 'Debye-Scherrer equation'. Nat Nanotechnol 6:534
33. Zhu X, Su Q, Feng W, Li F (2017) Anti-stokes shift luminescent materials for bio-applications. Chem Soc Rev 46:1025–1039
34. Goyal A, Soni PR (2018) Functionally graded nanocrystalline silicon powders by mechanical alloying. Mater Lett 214:111–114
35. Qian F, Li X, Tang L, Lai SK, Lu C, Lau SP (2016) Potassium doping: tuning the optical properties of graphene quantum dots. AIP Adv 6:075116–075124
36. Antaris AL, Chen H, Diao S, Ma Z, Zhang Z, Zhu S, Wang J, Lozano AX, Fan Q, Chew L, Zhu M, Cheng K, Hong X, Dai H, Cheng Z (2017) A high quantum yield molecule-protein complex fluorophore for near-infrared II imaging. Nat Comm 8:15269–15280
37. Kresse G, Furthmüller J (1996) Efficiency of ab-initio total energy calculations for metals and semiconductors using a plane-wave basis set. Comput Mater Sci 6:15–50
38. Kresse G, Furthmüller J (1996) Efficient iterative schemes for ab-initio total-energy calculations using a plane-wave basis set. Phys Rev B: Condens Matter 54:11169–11186
39. Kresse G, Hafner J (1993) Ab-initio molecular dynamics for liquid metals. Phys Rev B 47:558–561
40. Perdew JP, Burke K, Ernzerhof M (1996) Generalized gradient approximation made simple. Phys Rev Lett 77:3865–3868
41. Payne MC, Teter MP, Allan DC, Arias TA, Joannopoulos JD (1992) Iterative minimization techniques for ab-initio total-energy calculations: molecular dynamics and conjugate gradients. Rev Mod Phys 64:1045–1097
42. Heyd J, Scuseria GE, Ernzerhof M (2003) Hybrid functionals based on a screened coulomb potential. J Chem Phys 118:8207–8215
43. Heyd J, Scuseria GE (2004) Efficient hybrid density functional calculations in solids: assessment of the Heyd–Scuseria–Ernzerhof screened coulomb hybrid functional. J Chem Phys 121:1187–1192
44. Blöchl PE (1994) Projector augmented-wave method. Phys Rev B 50:17953–17979
45. Kresse G, Joubert D (1999) From ultrasoft pseudo potentials to the projector augmented-wave method. Phys Rev B 59:1758–1775
46. Monkhorst HJ, Pack JD (1976) Special points for brillouin-zone integrations. Phys Rev B 13:5188–5192
47. Qiao YB, Li YL, Zhong GH, Zeng Z, Qin XY (2007) Anisotropic properties of TaS_2. Chin Phys 16:3809–3815
48. Sanders CE, Dendzik M, Ngankeu AS, Eich A, Bruix A, Bianchi M, Miwa JA, Hammer B, Khajetoorians AA, Hofmann P (2016) Crystalline and electronic structure of single-layer TaS_2. Phys Rev B 94:081404–081408

Publisher's Note